

## AUTOMATED GLAUCOMA DETECTION USING HYBRID FEATURE EXTRACTION IN RETINAL FUNDUS IMAGES

M MUTHU RAMA KRISHNAN

*Department of Electronics and Computer Engineering  
Ngee Ann Polytechnic, Singapore 599489  
mkm2@np.edu.sg*

OLIVER FAUST

*School of Electronic Information Engineering  
Tianjing University  
fol2@np.edu.sg*

Received 31 May 2012

Revised 4 July 2012

Accepted 16 July 2012

Published 21 August 2012

Glaucoma is one of the most common causes of blindness. Robust mass screening may help to extend the symptom-free life for affected patients. To realize mass screening requires a cost-effective glaucoma detection method which integrates well with digital medical and administrative processes. To address these requirements, we propose a novel low cost automated glaucoma diagnosis system based on hybrid feature extraction from digital fundus images. The paper discusses a system for the automated identification of normal and glaucoma classes using higher order spectra (HOS), trace transform (TT), and discrete wavelet transform (DWT) features. The extracted features are fed to a support vector machine (SVM) classifier with linear, polynomial order 1, 2, 3 and radial basis function (RBF) in order to select the best kernel for automated decision making. In this work, the SVM classifier, with a polynomial order 2 kernel function, was able to identify glaucoma and normal images with an accuracy of 91.67%, and sensitivity and specificity of 90% and 93.33%, respectively. Furthermore, we propose a novel integrated index called Glaucoma Risk Index (GRI) which is composed from HOS, TT, and DWT features, to diagnose the unknown class using a single feature. We hope that this GRI will aid clinicians to make a faster glaucoma diagnosis during the mass screening of normal/glaucoma images.

**Keywords:** Glaucoma; retina imaging; computer aided diagnosis; higher order spectra; trace transform, texture; wavelet; support vector machine.

### Abbreviations

Acc accuracy  
ANN artificial neural network

AROC	area under the receiver operating curve
CWT	continuous wavelet transform
DWT	discrete wavelet transform
EEG	electroencephalography
FFT	fast Fourier transform
GLCM	gray level co-occurrence matrix
GRI	Glaucoma Risk Index
HOS	higher order spectra
HRT	Heidelberg retinal tomography
IMED	image Euclidean distance
IOP	intraocular pressure
LDA	linear discriminant analysis
NFT	nerve fibre thickness
ONH	optic nerve head
PCA	principal component analysis
PPA	peripapillary chorioretinal atrophy
PPV	positive predictive value
RBF	radial basis function
RFC	random-forest classifier
RNF	retinal nerve fibres
SLP	scanning laser polarimetry
Sn	sensitivity
Sp	specificity
SVM	support vector machine
TT	trace transform
WP	wavelet packet

1. Introduction

Glaucoma is one of the most common causes of blindness. The disease has a mean prevalence of 2.4% for all ages and 4.7% for those aged 75 and above.<sup>1</sup> It is estimated that more than 4million Americans suffer from glaucoma, and half of them are unaware that they have the disease. Approximately 120,000 Americans are blind as a result of glaucoma, consequently making it responsible for 9–12% of all cases of blindness in the United States.<sup>2</sup> Much of this suffering is preventable, because preventive medicine and surgical treatment, such as mean trabeculectomy, laser surgery, drainage implants, are available. Unfortunately, glaucoma symptoms are painless and the brain compensates gradual vision impairment to a considerable extent. Therefore, early diagnosis is important to stop or slow down disease progression. However, due to the high mean prevalence of

glaucoma, a significant reduction of end stage glaucoma and blindness requires mass screening.<sup>3</sup>

Glaucoma leads to (1) structural changes of the optic nerve head (ONH) and the nerve fibre layer and (2) simultaneous functional failure of the visual field. The disease is diagnosed based on intraocular pressure (IOP), visual field loss tests,<sup>4,5</sup> and the manual assessment of the ONH via ophthalmoscopy<sup>3</sup> or stereo fundus imaging.<sup>6</sup> Various algorithms have been used to identify typical features such as abnormality of blood vessels<sup>7</sup> and ONH,<sup>8,9</sup> location and quantification of microaneurisms or drusen.<sup>10–12</sup> State-of-the-art glaucoma diagnosis is based on Heidelberg retinal tomography (HRT) images. Swindale *et al.* and Adler *et al.* have modeled a smooth two-dimensional (2D) surface that fit to the ONH of topography images.<sup>13,14</sup> Damage in the glaucomatous eye was detected using optic disk measures (cup and disk area, height variation using HRT images).<sup>15</sup> This global shape approach was compared with a sector-based analysis by Lester *et al.*<sup>16</sup> Zangwill *et al.* have automatically diagnosed glaucoma using optic disk parameters, additional parapapillary parameters, and the support vector machine (SVM) classifier.<sup>17</sup> Most of these shape approaches assume a valid segmentation of the optic disk. However, a small error in these segmentation-based techniques may result in significant changes in the measurements and errors in the diagnosis. Furthermore, HRT imaging is an expensive measurement, because both manpower and equipment cost are high. Currently, state-of-the-art glaucoma detection requires mass screening. Hence, the number of measurements is potentially very high and a small cost reduction per measurement will make a large difference.

We attempt to achieve such a small cost reduction by proposing a glaucoma diagnosis system based on hybrid feature extraction from digital fundus images. The cost reduction comes from the fact that digital fundus images are less expensive as compared to HRT and feature extraction is done with inexpensive general purpose computing machines. Furthermore, both processes (image taking and feature extraction) occur in the digital domain, therefore the proposed glaucoma diagnosis system can be easily incorporated into existing medical and administrative workflows. These advantages do not constrain the reliability of the diagnosis support system. To be specific, we show that the proposed system is able to differentiate fundus images from glaucoma patients from those of a normal control group with an accuracy of 91.67%. Furthermore, we propose a novel integrated index, called the Glaucoma Risk Index (GRI), which is made up of higher order spectra (HOS), trace transform (TT), and discrete wavelet transform (DWT) features, to diagnose the unknown class using a single feature.

The layout of the paper is as follows: Section 2 explains the materials and methods used for this study. Section 3 of the paper discusses the hybrid feature extraction methods. Section 4 of the paper presents the SVM classification. The GRI is explained in Sec. 5. The results of the proposed method presents in Sec. 6. The results are discussed in Sec. 7 and finally, the paper is concluded in Sec. 8.

2. Materials and Methods

Figure 1 shows a block diagram of the proposed system. During the preprocessing stage, colored images are converted to grayscale images and the image contrast is increased with histogram equalization. The Radon transformation converts 2D images into one-dimensional (1D) signals. After these preprocessing steps, important features, namely, phase entropy, bispectrum entropy using HOS, triple feature using T1, and average energy of wavelet coefficients are extracted from the image.

The statistical significance of these features is evaluated with the independent sample *t*-test. To evaluate the discriminative powers of these features in a practical setting, they were fed to an SVM classifier for automated diagnosis support.

2.1. Retinal fundus image acquisition

The digital retinal images were collected from the Kasturba Medical College, Manipal, India. We have used 60 fundus images — 30 normal and 30 open-angle glaucoma images from male and female participants who were between 20 and 70 years old. The doctors in the hospital’s Ophthalmology Department certified both

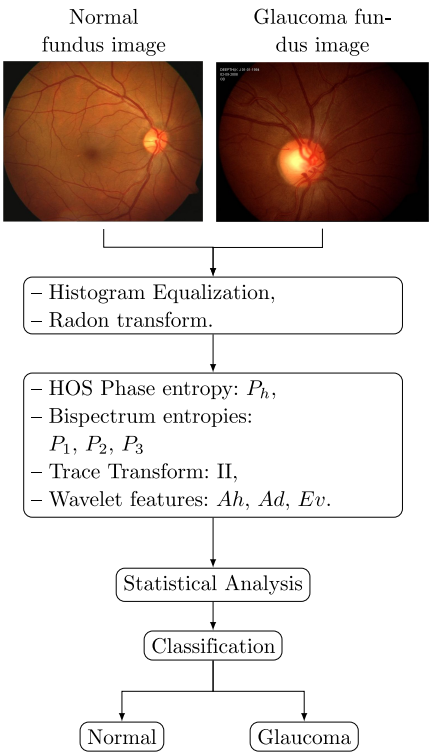


Fig. 1. Block diagram of the proposed automated glaucoma detection system.

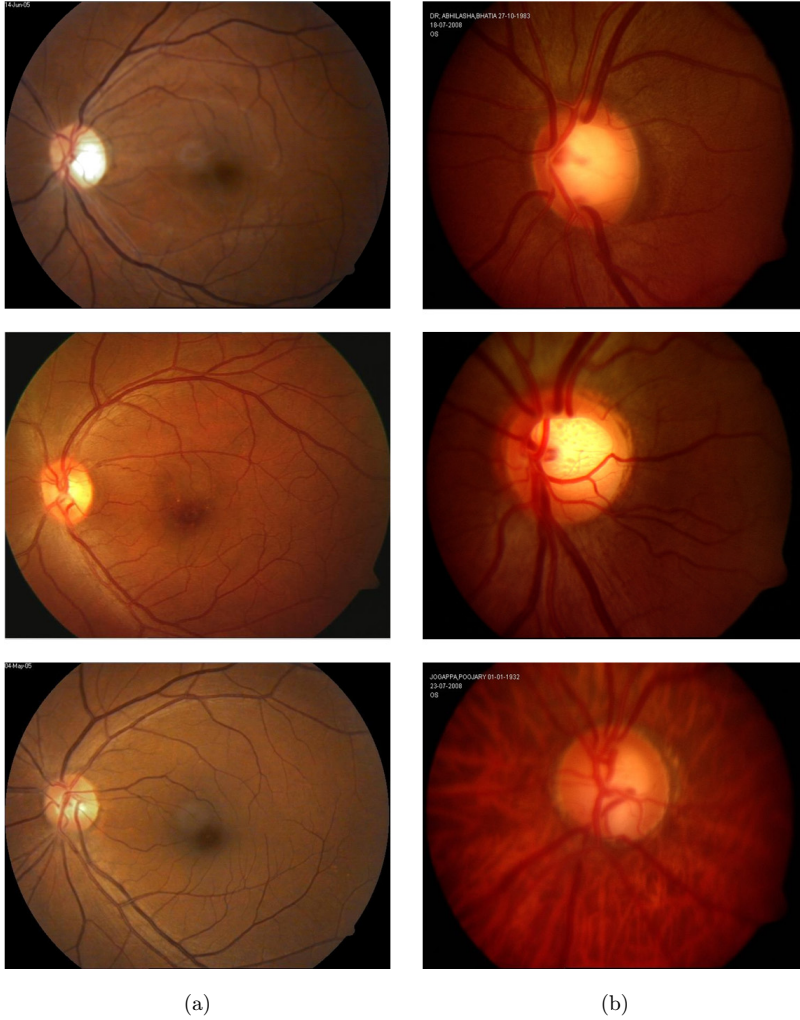


Fig. 2. Representative images: Column-(a): Normal; Column-(b): Glaucoma.

image quality and usability. The ethics committee, consisting of senior doctors, approved the images for this research. All images were taken with a resolution of  $560 \times 720$  pixels and stored in the uncompressed bitmap format. Figure 2 shows representative normal and glaucoma sample images to highlight texture variations between the two groups.

## 2.2. Preprocessing

Preprocessing involves two major steps: (1) histogram equalization and (2) Radon transformation.

2.2.1. Histogram equalization

Enhancing the fundus image contrast will aid the feature extraction process. In this work, colored (RGB) eye images are converted to grayscale images by forming a weighted sum of the R, G, and B components using Eq. (1):

$$I_{\text{gray}} = 0.2989 \times R + 0.5870 \times G + 0.1140 \times B. \tag{1}$$

Then, the contrast is improved by increasing the dynamic range of the image histogram.<sup>18</sup> This technique assigns pixel intensity values from an input image such that the output image contains a uniform distribution of intensities. As a result, the image contrast is increased. We have used images with good contrast to model a histogram (Fig. 3(a)). This modelled histogram (Fig. 3(c)) is considered as a standard and given as an input to the histogram equalization procedure. Finally, we obtained the histogram-equalized image (Fig. 3(g)).

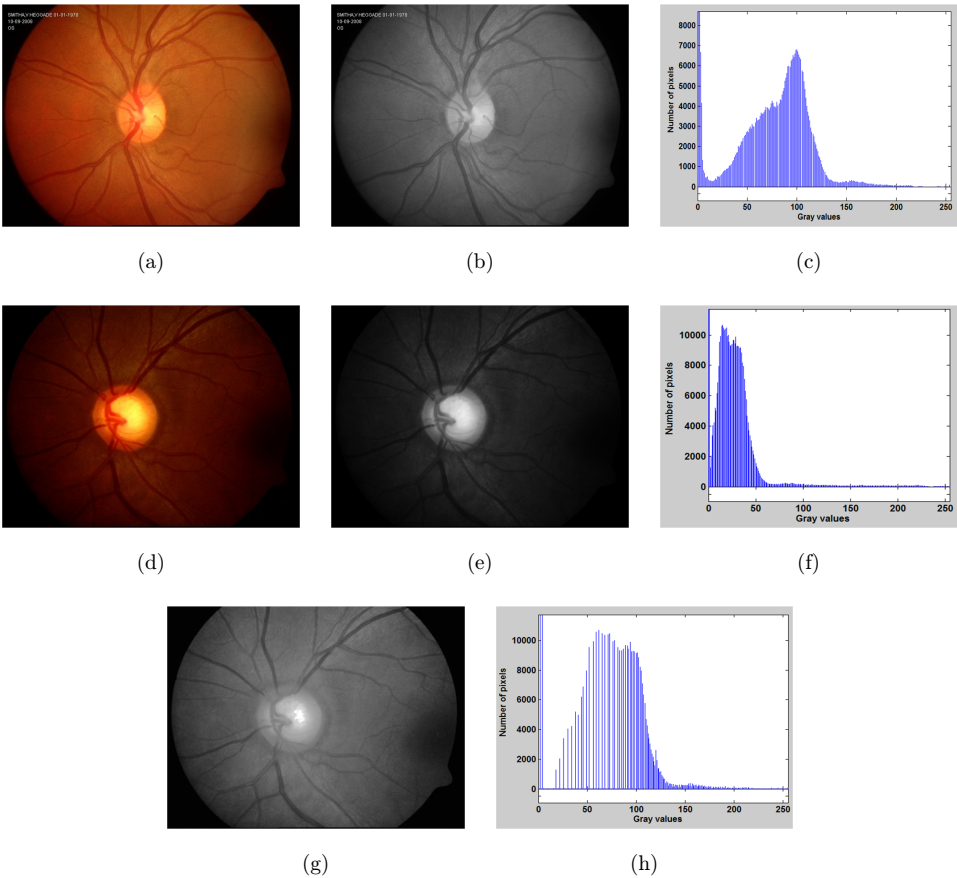


Fig. 3. (a) Standard reference image for histogram equalization, (b) grayscale image of (a), (c) histogram of image (b), (d) original glaucoma image, (e) grayscale image of (d), (f) histogram of image (e), (g) histogram equalized image of (e), and (h) histogram of image (g).

### 2.2.2. Radon transform

TT methods, such as Radon transform, yield many useful features with minimal computational requirements.<sup>19</sup> These features may be devoid of any physical meaning according to human perception, but they can have the right mathematical properties which are able to distinguish objects.

The Radon transform is widely used in computed tomography to create an image from scattering data which is associated with cross-sectional scans of an object. It transforms 2D images with lines into a domain of possible line parameters, where each line in the image will give a peak that is positioned to reflect the corresponding line parameters.<sup>20</sup> Hence, lines in the original image are transformed into points in the Radon domain. The glaucoma image (Fig. 3(g)) is subjected to Radon transform with angles varying from 0–180° (with 5° interval). Figure 4 shows the results of the Radon transform for 30°, 90°, and 150°.

## 3. Feature Extraction

Texture analysis is used in retinal fundus and ultrasound images to diagnose glaucoma, thyroid, and vascular abnormalities.<sup>4,21–25</sup> Peripapillary chorioretinal atrophy is considered as one of the glaucoma risk factors. It can be identified as bright regions in retinal fundus images.

### 3.1. Higher order spectra-based features

HOS techniques were first applied to signal processing problems in 1970; subsequently, they were used in economics, speech, seismic data processing, plasma

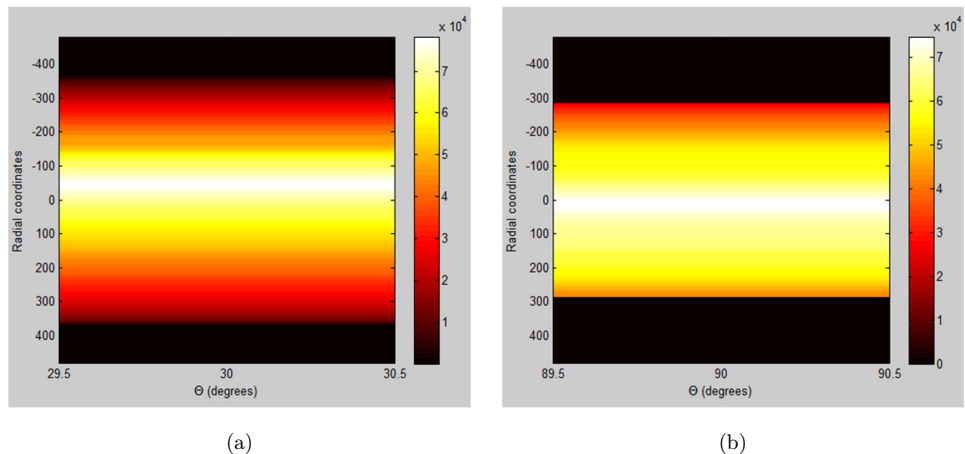


Fig. 4. (a) Radon transform image with angle 30°, (b) Radon transform image with angle 90°, and (c) Radon transform image with angle 150°.

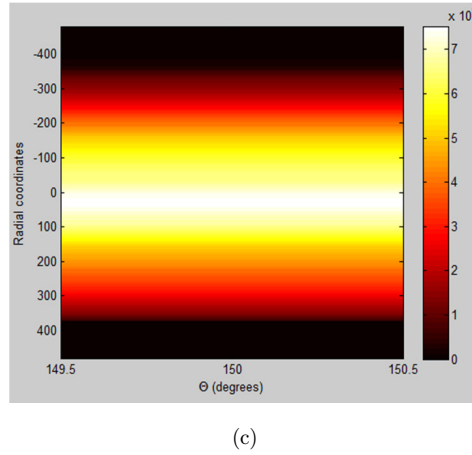


Fig. 4. (Continued)

physics, optics, and biomedical applications.<sup>20,26</sup> Recent studies show that HOS can be used to diagnose epilepsy using electroencephalography (EEG) signals and cardiac abnormalities using heart rate signals.<sup>27,28</sup> HOS invariants have been used for shape recognition<sup>29</sup> and to identify different kinds of eye diseases.<sup>4,20</sup>

HOS is a nonlinear method which captures subtle changes in image pixels. The algorithm discussion starts with second order statistics which evaluate both mean value ( $m$ ) and variance ( $\sigma^2$ ). They are defined by expectation operation as follows (where “ $a$ ” is the result of a random process):

$$\begin{aligned} m_a &= \mathbb{E}\{A\} \text{ and} \\ \sigma_A^2 &= \mathbb{E}\{(A - m_a)^2\}. \end{aligned} \quad (2)$$

If  $a$  is a time discrete signal, the second order moment autocorrelation function is defined as:

$$m_a^2(i) = \mathbb{E}\{(A(n) \times A(n+1))\}. \quad (3)$$

In addition to these moments, HOS provides higher order moments, i.e.,  $m3$ ,  $m4, \dots$  and nonlinear combinations of the higher order moments called “cumulants”, i.e.,  $c1, c2, c3, \dots$ . Thus, HOS consists of both moment and cumulant spectra.<sup>27,28</sup> The technique can be used for deterministic and random signals. The so-called “bispectrum”, which is a third order statistic, was used in this work. It is obtained by calculating the Fourier transform of the third order correlation of the data:

$$B(f_1, f_2) = \mathbb{E}\{A(f_1) A(f_2) A^*(f_1 + f_2)\}, \quad (4)$$

where  $A(f)$  is the Fourier transform of the signal  $a(nT)$  and  $\mathbb{E}\{\cdot\}$  is an average over an ensemble of random signal realizations. For deterministic signals, the relationship holds without an expectation operation. In this case, the third order correlation is a



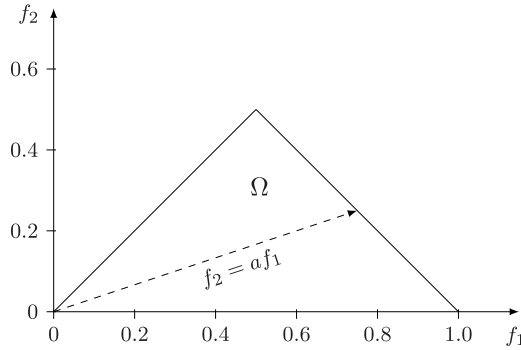


Fig. 5. Non-redundant region of computation of the bispectrum for real signals. Features are calculated by integrating the bispectrum along the dashed line with slope =  $a$ . Frequencies are shown normalized by the Nyquist frequency.

time-average. For deterministic sampled signals,  $A(f)$  is the discrete-time Fourier transform, which, in practice, is computed using the fast Fourier transform (FFT) algorithm. The frequency ( $f$ ) may be normalized by the Nyquist frequency to be between 0 and 1 (Fig. 5).

In this work, we derived the bispectral phase entropy ( $P_h$ ), entropy 1 ( $P_1$ ), entropy 2 ( $P_2$ ), and entropy 3 ( $P_3$ ). These entropies are similar to the spectral entropy.<sup>27,28</sup> The equations, which govern the phase entropy extraction from HOS parameters, are given below:<sup>20</sup>

$$P_h = \sum_{\langle n \rangle} p(\Psi_n) \log(p(\Psi_n)), \quad (5)$$

$$p(\Psi_n) = \frac{1}{L} \sum_{\langle \Omega \rangle} l(\Phi(B(f_1 f_2)) \in \Psi_n), \quad \text{and} \quad (6)$$

$$\Psi_n = \{\Phi | -\pi + 2\pi n/N \leq \Phi < -\pi + 2\pi(n+1)/N\} \\ \text{with } n = 0, 1, \dots, N-1, \quad (7)$$

where  $B$  indicates the bispectrum of the signal,  $L$  is the number of points within the region  $\Omega$ ,  $\Phi$  is the phase angle of the bispectrum, and  $l(\cdot)$  is an indicator function which gives a value of 1 when the phase angle is within the range of  $\Psi_n$ , as depicted by in Eq. (6). The three bispectrum entropies are defined as:

$$P_1 = - \sum_{\langle k \rangle} p_k \log(p_k), \quad (8)$$

where  $p_k = \frac{|B(f_1, f_2)|}{\sum_{\langle \Omega \rangle} |B(f_1, f_2)|}$ ;

$$P_2 = - \sum_{\langle i \rangle} p_i \log(p_i), \quad (9)$$

where  $p_i = \frac{|B(f_1, f_2)|^2}{\sum_{\langle \Omega \rangle} |B(f_1, f_2)|^2}$ ; and

$$P_3 = - \sum_{\langle n \rangle} p_n \log(p_n), \quad (10)$$

where  $p_n = \frac{|B(f_1, f_2)|^3}{\sum_{\langle \Omega \rangle} |B(f_1, f_2)|^3}$ .

In this work, we extracted the four bispectrum invariants, described above, for each Radon-transformed fundus image.

### 3.2. Trace transform (TT)

TT is a generalized approach to the Radon transform, and consists of tracing an image with straight lines along certain functionals of the so-called “image function”. The purpose of a functional is to characterize a function by a number. Different functionals are used to represent rotation, translation, and scaling invariant features of an image. In many cases, these features correlate well with the visual textures.<sup>19</sup>

The TT can then be defined as a function  $g$  based on  $\Delta$  with the help of  $T$ , which is some functional of the image function with variable  $t$ .  $T$  is called the trace functional. In order to define a triple feature, two more functionals have been defined and they are designated by  $P$  and  $\Phi$ .<sup>19</sup>  $P$  is known as the diametrical functional, which is a functional of the TT function when it is considered as a function of the length of the normal to the line only.  $\Phi$ , called the circus functional, is a functional operating on the orientation variable, after the previous two operations ( $T$  and  $P$ ) have been performed. Thus, the triple feature can be defined as:

$$\Pi = (F, C_1) = \Phi(P(T(F(C_1, \Phi, p, t)))), \quad (11)$$

where  $F(C_1, \Phi, p, t)$  indicates the values of the image function along the chosen line.  $C_1$  is the coordinate system which is parameterized by  $(\Phi, p, t)$ . We calculate two triple features using the invariant functionals. They are as follows:

$$\begin{aligned} \Pi_1 &= T \rightarrow IF_1, \quad P \rightarrow IF_2, \quad \Phi \rightarrow IF_3, \quad \text{and} \\ \Pi_2 &= T \rightarrow IF_3, \quad P \rightarrow IF_2, \quad \Phi \rightarrow IF_1, \end{aligned} \quad (12)$$

where  $\Pi_1$  is the normalized version of the triple feature formed by using  $IF_1$ ,  $IF_2$ , and  $IF_3$  as functionals  $T$ ,  $P$ , and  $\Phi$ , respectively in Eq. (11).  $\Pi_2$  is the normalized version of the triple feature formed by  $IF_3$ ,  $IF_2$ , and  $IF_1$  as functionals  $T$ ,  $P$ , and  $\Phi$ , respectively in Eq. (11).  $\Pi_1$  and  $\Pi_2$  are the rotation, scale, and translation invariant texture features that are used to quantify a visual texture measure in our application.

### 3.3. Discrete wavelet transform energy features

Wavelets are mathematical functions that decompose data into different frequency components and subsequently study each component with a resolution which is matched to its scale. The Fourier transform decomposes a signal into a spectrum of frequencies, whereas the wavelet analysis decomposes a signal into a hierarchy of scales starting from the coarsest scale.<sup>30</sup> This ability to represent an image at various

resolutions makes the wavelet transform a better tool for extracting features from images than the Fourier transform.<sup>31,32</sup> Multiresolution analysis can be done using continuous wavelet transforms (CWT) and DWT. In our work, we have used DWT for feature extraction, which is explained below.

The DWT transform of a 2D signal  $x(n)$  is evaluated by sending it through a sequence of down-sampling high and low-pass filters.<sup>33</sup> The low-pass filter is defined by the transfer function  $L(n)$  and the high-pass filter is defined by the transfer function  $H(n)$ . The output of the high-pass filter  $D(n)$  is known as the detailed coefficients. The following equation shows how these coefficients are obtained:

$$D(n) = \sum_{k=-\infty}^{\infty} x(k) H(2n - k). \quad (13)$$

The low-pass filter output is known as the approximation coefficients. These coefficients are found by using the following equation:

$$A(n) = \sum_{k=-\infty}^{\infty} x(k) L(2n - k). \quad (14)$$

The frequency resolution is further increased by cascading the two basic filter operations. To be specific, the output of the first level low-pass filter is fed into the same low- and high-pass filter combination. The detailed coefficients are output at each level and they form the level coefficients. In general, each level halves the number of samples and doubles the frequency resolution. Consequently, in the final level, both detailed and approximation coefficients are obtained as level coefficients.

In our work, the digital fundus images are represented as an  $m \times n$  grayscale matrix  $I(i, j)$ , where each element of the matrix represents the intensity of one pixel. All non-border pixels  $I(i, j)$ , where  $i \notin \{0, m\}$  and  $j \notin \{0, n\}$ , have eight immediate neighboring pixels. These eight neighbors can be used to traverse through the matrix.<sup>34</sup> However, changing the direction with which the matrix is traversed just inverts the sequence of pixels and the 2D DWT coefficients are the same. For example, the wavelet packet (WP) result is the same when the matrix is traversed from left to right as from right to left. Therefore, we are left with four possible directions, which are known as decomposition corresponding to  $0^\circ$  (horizontal,  $Dh$ ),  $90^\circ$  (vertical,  $Dv$ ), and  $45^\circ$  or  $135^\circ$  (diagonal,  $Dd$ ) orientations.

In this work, level 1 decomposition was sufficient to obtain significant features. We have evaluated 54 wavelet functions. Each of these wavelet functions has a unique low-pass filter transfer function  $L(n)$  and a unique high-pass filter transfer function  $H(n)$ .<sup>33</sup> We found that Biorthogonal 3.1 (bior3.1) outperforms all other tested wavelet functions. Biorthogonal is the name of a wavelet where the associated wavelet transform is invertible but not necessarily orthogonal. Biorthogonal wavelets allow more degrees of freedom than orthogonal wavelets.

The first level 2D DWT yields four resultant matrices, namely  $Dh_1$ ,  $Dv_1$ ,  $Dd_1$ , and  $A_1$ , whose elements are intensity values. The following average and mean value equations were used to extract features from the resultant DWT matrices:

$$\begin{aligned}
 \text{Average } Dh_1(Ah) &= \frac{1}{N \times M} \sum_{x=\langle N \rangle} \sum_{y=\langle M \rangle} |Dh_1(x, y)|, \\
 \text{Average } Dv_1(Av) &= \frac{1}{N \times M} \sum_{x=\langle N \rangle} \sum_{y=\langle M \rangle} |Dv_1(x, y)|, \\
 \text{Average } Dd_1(Ad) &= \frac{1}{N \times M} \sum_{x=\langle N \rangle} \sum_{y=\langle M \rangle} |Dd_1(x, y)|, \\
 \text{Energy } (Ed) &= \frac{1}{N^2 \times M^2} \sum_{x=\langle N \rangle} \sum_{y=\langle M \rangle} (Dd_1(x, y))^2, \quad \text{and} \\
 \text{Energy } (Ev) &= \frac{1}{N^2 \times M^2} \sum_{x=\langle N \rangle} \sum_{y=\langle M \rangle} (Dv_1(x, y))^2.
 \end{aligned} \tag{15}$$

#### 4. Support Vector Machine

The number of medical diagnosis systems, which use automated classification, is gradually increasing.<sup>35</sup> The evaluation of patient data and decisions by medical experts are the most important factors in diagnosis. Classification systems can help to minimize possible errors and they can provide examination results in a shorter time and in a more detailed manner. In this study, the diagnostic problem is designed based on 14 features of retinal fundus images, which may be treated as a two-class pattern classification problem.

The SVM algorithm is based on the idea of margin maximization.<sup>35–37</sup> The maximum margin can be found by solving the following optimization problem:

$$\begin{aligned}
 \min \left\{ \frac{1}{2} w^T w + C \sum_{i=1}^l \xi_i^2 \right\} \\
 \text{s.t. } y_i(w^T x_i + b) \geq 1 - \xi, \quad \text{where } i = 1, \xi \geq 0.
 \end{aligned} \tag{16}$$

The decision function for linear SVMs is given as  $g(x) = w^T x + b$ . In this formulation, we have the training data set  $\{x_i, y_i\}$ ,  $i = 1, \dots, l$ , where  $x_i \in R^n$  are the training data points,  $y_i$  is the class label,  $l$  is the number of samples, and  $n$  is the number of features in each sample. By solving the optimization problem presented in Eq. (16), i.e., by finding the parameters  $w$  and  $b$  for a given training set, we are effectively designing a decision hyperplane (Fig. 6) over an  $n$  dimensional input space that produces the maximal margin in the space. Generally, the optimization problem, defined in Eq. (16), is solved by changing it into the dual problem, as given

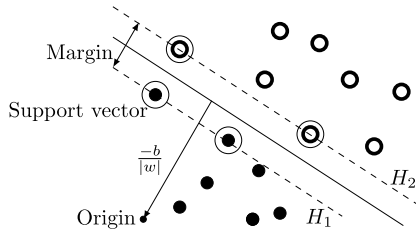


Fig. 6. Optimal separating hyperplanes.

below:

$$\max\{L_d(\alpha)\} = \sum_{i=1}^l \alpha_i - \frac{1}{2} \sum_{i,j=1}^l y_i y_j \alpha_i \alpha_j x_i^T x_j. \quad (17)$$

Subject to  $0 \leq \alpha_i \leq C_i$ , where  $i = 1, \dots, l$ :

$$\sum_{i=1}^l \alpha_i y_i = 0. \quad (18)$$

In this setting, one needs to maximize the dual objective function  $L_d(\alpha)$  with respect to the dual variables  $\alpha_i$  only subject to the box constraints  $0 \leq \alpha_i \leq C$ . The optimization problem can be solved by various established techniques which solve general quadratic programming problems with inequality constraints. The original optimal hyperplane algorithm was a linear classifier. This linear algorithm can be made nonlinear by replacing every dot product by a nonlinear kernel function, such as the radial basis function (RBF).

## 5. Glaucoma Risk Index

We have formulated the GRI based on the significant features listed in Table 1. Our approach follows that of Acharya *et al.*, who have proposed to combine features in such a way that the resulting number or index discriminates normal and disease classes.<sup>24</sup> It is difficult keep track of the individual feature variations. Therefore, we have empirically determined a single integrated index (also called GRI) that is a unique combination of the respective features that results in a unique range for both the classes. The utility of such indices is that they can be more comprehensible to the ophthalmologist than the classifiers which are most times black boxes that directly output the class label. Moreover, it is faster and easier to compute and keep track of these indices. When continuously monitored, the variations in the indices can throw light on how the normal become glaucoma over time. In our case, the GRI discriminates fundus images which show glaucoma symptoms from normal fundus images.

Equation (19) describes how the features were combined to form the GRI.

$$\text{GRI} = \frac{\alpha}{\beta \times \gamma} \quad (19)$$

Table 1. Summary of features used in this work.

Features	Normal	Glaucoma	<i>p</i> -value
$P_1$ (0°)	0.5022 ± 0.1874	0.3834 ± 0.0851	0.002502
$P_h$ (70°)	1.5415 ± 0.7583	2.2898 ± 1.0185	0.002055
$P_h$ (75°)	1.5768 ± 0.7353	2.187 ± 0.778	0.002797
$P_h$ (80°)	1.7648 ± 0.7481	2.3864 ± 0.7448	0.002069
$P_h$ (85°)	1.9665 ± 0.6708	2.5781 ± 0.6274	0.000569
$P_h$ (90°)	0.5675 ± 0.2007	0.4495 ± 0.0607	0.003134
$P_1$ (90°)	0.1222 ± 0.0768	0.0743 ± 0.0309	0.00244
$P_2$ (90°)	0.0405 ± 0.0257	0.0212 ± 0.0153	0.000781
$P_3$ (90°)	2.9489 ± 0.4061	3.273 ± 0.3483	0.001572
$P_1$ (180°)	0.5129 ± 0.1995	0.3757 ± 0.0801	0.000912
TT1	2.6728 ± 0.5147	2.4491 ± 0.2142	0.031949
<i>Ah</i>	2.6243 ± 0.9351	1.8899 ± 0.1584	8.10E-05
<i>Ad</i>	2.068 ± 0.7291	1.6534 ± 0.1454	3.40E-03
<i>Ev</i>	0.0001 ± 0.0002	0.0007 ± 0.0003	1.06E-14

with

$$\begin{aligned}\alpha &= P_1(0^\circ) \times P_h(70^\circ) \times P_h(75^\circ) \times P_h(80^\circ) \times P_h(85^\circ) \\ &\quad \times P_h(90^\circ) \times P_1(90^\circ) \times P_2(90^\circ) \times P_3(90^\circ) \times P_1(180^\circ) \\ \beta &= Ah \times Ad \times Ev \\ \gamma &= TT_1,\end{aligned}\tag{20}$$

where  $\alpha$  indicates the combination of HOS features,  $\beta$  indicates the combination of wavelet features, and  $\gamma$  indicates the combination of trace transform features.

6. Results

In this study, we have used TT, HOS, and DWT, methods to extract 14 features from digital fundus images. The independent sample *t*-test was used to establish the statistical significance of these features. Table 1 shows mean, standard deviation and *p*-value of the extracted features. All features, with the exception of  $P_1$ , showed significantly greater values in images taken from glaucomatous participants when compared to the normal control set (Table 1,  $p < 0.01$ ). The low *p*-values indicate that all features are extremely useful in differentiating normal images from retinal images with glaucomatous appearance. In the case of HOS-based features, bispectral entropy based features which, were obtained from Radon transform angles  $\Theta = 0^\circ, 70^\circ, 75^\circ, 80^\circ, 85^\circ, 90^\circ$ , and  $180^\circ$ , were found to be statistically significant. Among the TT features,  $\Pi_1$  was found to statistically significant. Finally, the DWT features *Ad*, *Av*, and *Ev*, based on bior3.1, were found to be statistically significant.

Table 2 shows that the GRI is a highly efficient indicator of the difference between normal and glaucomatous cases. The index can also be employed as an adjunct tool to cross check the diagnosis of clinicians using just one number. Figure 7 shows the distribution plot of the GRI for normal and glaucoma. This plot graphically

Table 2. Range of GRI for normal and glaucoma datasets.

Feature	Normal	Glaucoma	$p$ -value
GRI	$12.41 \pm 0.024$	$1.92 \pm 0.017$	$< 0.0001$

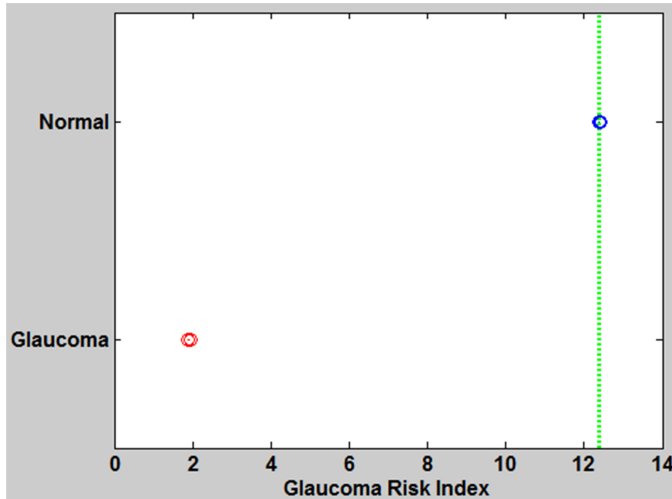


Fig. 7. Plot of GRI for normal and glaucoma classes.

documents how well this integrated index separates the normal control group from patients with glaucoma.

The computation of GRI is performed using phase entropy ( $P_h$ ), bispectrum entropies ( $P_1$ ,  $P_2$ ,  $P_3$ ) and wavelet energy features ( $Ah$ ,  $Ad$ , and  $Ev$ ). The wavelet energy values of glaucoma are low, this effect may indicate a degeneration of the optic nerve (Table 1), which are expressed as  $\beta$ . The phase entropy values of HOS are high in case of glaucoma, which are expressed as  $\alpha$ . The higher values of HOS features and lower values of wavelet energy features suggest that glaucoma fundus images with glaucoma symptoms have a more coarse textural variation than normal ones. In the case of optic nerve hemorrhages, the blood typically collects along the individual nerve fibres that radiate outward from the nerve. Such physiological changes are manifested in fundus images and our experiments show that HOS and DWT features are able to detect and quantify such differences in the eye physiology.<sup>4</sup>

In this work, the so-called “three-fold stratified cross validation” method was used to test the classifiers. Two parts of the data (training set) were used for classifier development and one part (test set) is used to test the classifier (i.e., 40 images were used for training and 20 images were used for testing). This procedure was repeated three times using a different part as the test set in each case. The average of the

Table 3. Results of SVM classification.

SVM kernels	TN	FN	TP	FP	Acc	PPV	Sn	Sp
Linear	10	1	9	0	91.67%	96.67%	86.67%	96.67%
Polynomial degree 2	9	1	9	1	91.67%	93.94%	90%	93.33%
Polynomial degree 3	9	1	9	1	88.33%	88.6%	90%	86.67%
RBF	9	1	9	1	90%	92.96%	86.67%	93.33%

accuracy (Acc), sensitivity (Sn), specificity (Sp), and positive predictive value (PPV) was calculated for all three trials to obtain the overall performance measures. Table 3 presents the classification results obtained using significant HOS, TT, and DWT features from the retinal fundus images. The accuracy registered by SVM with polynomial and linear kernel was 91.67%.

7. Discussion

Table 4 presents a summary of the automated glaucoma detection studies which were mentioned in this paper. Many studies have been conducted to develop computer aided decision support systems for the early detection of glaucoma. An artificial neural network (ANN) model, using multifocal visual evoked potential (M-VEP) data, was able to detect glaucoma with a high sensitivity and specificity of 95% and 94%, respectively.<sup>38</sup>

The performance of an ANN to recognize glaucomatous visual field defects, was studied and its diagnostic accuracy was compared with that of other algorithms which were proposed for the detection of visual field loss.<sup>39</sup> The ANN method showed a sensitivity of 93%, specificity of 94% and an area under the receiver operating curve (AROC) curve of 0.984. The cluster algorithm achieved a sensitivity of 95% and specificity of 82%.

Nayak *et al.* have proposed a morphological image processing algorithm based on fundus images to detect glaucoma symptoms. The authors used the cup-to-disk (c/d) ratio, which indicates the distance between the cup portion of the ONH to the diameter of the optic disk, and the ratio of blood vessels area in inferior–superior side to area of blood vessel in the nasal–temporal side considered as features to design a neural network.<sup>40</sup> Their system was able to identify glaucoma with a sensitivity and specificity of 100% and 80%, respectively. A new framework for the detection of glaucoma based on the changes in the ONH, using the method of proper orthogonal decomposition, was proposed.<sup>41</sup> Any glaucomatous changes present in the ONH, during follow-up examinations, were estimated by comparing follow-up ONH topography with its baseline topograph subspace representation that was constructed earlier. The changes in the ONH were quantified using the following image correspondence measures: L1-norm and L2-norm, correlation, and image Euclidean distance (IMED). By using both L2-norm and IMED in the new framework, a AROC of 0.94 was achieved at 10° field of imaging, and 0.91 at 15° field of imaging.<sup>41</sup>



Table 4. Summary of automated glaucoma detection techniques used in this study.

Authors	Features	Classifier	Performance
Classification using morphological features of the retinal fundus images			
Nagarajan <i>et al.</i> (2002) <sup>38</sup>	Multi-focal visual evoked potential	ANN	Sensitivity: 95%
Bizios <i>et al.</i> (2007) <sup>39</sup>	ONH parameters	ANN	Sensitivity: 93%
		Cluster algorithm	Specificity: 94%
			Sensitivity: 95%
			Specificity: 82%
Nayak <i>et al.</i> (2009) <sup>40</sup>	Optic disk parameters	ANN	Sensitivity: 100%
	Blood vessel parameters		Specificity: 80%
Balasubramanian <i>et al.</i> (2009) <sup>41</sup>	ONH parameters	Proper orthogonal decomposition	AROC: 0.94
Huang <i>et al.</i> (2010) <sup>42</sup>	Retinal nerve fibre thickness	LDA	AROC: 0.95
		ANN	AROC: 0.97
Classification using texture features of the retinal fundus images			
Bock <i>et al.</i> (2007) <sup>43</sup>	PCA, FFT, and Spline interpolation data	SVM	Accuracy: 86%
Kolar and Jan (2008) <sup>45</sup>	Fractal dimension of RNF	SVM	Accuracy: 74%
Nyul (2009) <sup>3</sup>	Pixel intensities, FFT, and B-Spline	SVM	Accuracy: 80%
Acharya <i>et al.</i> (2011) <sup>4</sup>	Texture and HOS	RFC	Accuracy: 91%
Muramatsu <i>et al.</i> (2011) <sup>44</sup>	GLCM features	LDA	Sensitivity: 73%
			Specificity: 95%
Dua <i>et al.</i> (2012) <sup>33</sup>	Wavelet	RFC	Accuracy: 93%
Mookiah <i>et al.</i> (2012) <sup>5</sup>	HOS and DWT	SVM	Accuracy: 95%
This study	HOS, TT, DWT, and Energy features	SVM	Sensitivity: 90%
			Specificity: 93.33%
			Accuracy: 91.67%

Linear discriminant analysis (LDA) and an ANN were used to improve the differentiation between glaucomatous and normal eyes in a Taiwan–Chinese population based on the retinal nerve fibre layer thickness measurement data from the scanning laser polarimetry (SLP) with variable corneal compensation.<sup>42</sup> The results showed that the nerve fibre thickness (NFT) parameter produced the highest AROC of 0.932 in differentiating between normal and glaucomatous eyes. The AROC for the LDA and ANN methods were 0.950 and 0.970, respectively. Hence, the NFT, ANN, and LDF methods demonstrated equal diagnostic power in glaucoma detection.

Principal component analysis (PCA) was performed on pixel intensity values. Subsequently, FFT coefficients and spline interpolation data of digital fundus images were used to detect the glaucoma.<sup>43</sup> With an SVM classifier, the investigators obtained an accuracy of 86%.

The gray level co-occurrence matrix (GLCM) was used for the computerized detection of moderate to severe peripapillary chorioretinal atrophy (PPA). Mar- amatsu *et al.* obtained a sensitivity and specificity of 73% and 95%, respectively.<sup>44</sup>

The gradual loss of the retinal nerve fibres (RNF) is a glaucoma symptom with high diagnostic value. The texture changes in color or grayscale retinal photographs indicate the RNF atrophy.<sup>45</sup> The automated system using fractal and power spectral features coupled with SVM classifier was able to classify the normal and glaucoma groups with an accuracy of 74%.

Nyúl proposed automated glaucoma detection using fundus image features. Initially, variations, such as non-uniform illumination, size differences, and blood vessels were eliminated from the images. Then, PCA was applied in the combined features (Pixel intensities, FFT coefficients, and B-Spline coefficients).<sup>3</sup> These PCA coefficients, combined with a classifier, were able to achieve an accuracy of 80% for detecting glaucomatous retina fundus images.

Acharya *et al.*<sup>4</sup> proposed a method for glaucoma detection using a combination of texture and HOS features from digital fundus images. SVM, sequential minimal optimization, naïve Bayesian, and random-forest classifiers are used to perform supervised classification. The author demonstrated that the texture and HOS features after *z*-score normalization and feature selection, and when combined with a random-forest classifier (RFC), performs better than the other classifiers and correctly identifies the glaucoma images with an accuracy of more than 91%.

Dua *et al.*<sup>33</sup> proposed a technique to extract energy signatures obtained using 2D DWT, and subject these signatures to different feature ranking and feature selection strategies. The authors gauged the effectiveness of the resultant ranked and selected subsets of features using SVM, sequential minimal optimization, random forest, and naive Bayes classification strategies. The authors obtained an accuracy of around 93% using 10-fold cross validations.

Mookiah *et al.*<sup>5</sup> proposed the system for the automated identification of normal and glaucoma classes using HOS and DWT features. The automated system using HOS and DWT features with an SVM classifier was able to identify the glaucoma and normal images automatically with an accuracy of 95%, sensitivity and specificity of 93.33% and 96.67%, respectively.

In our present work, we were able to detect the normal and glaucoma classes with accuracy of 91.67%, sensitivity of 90%, and specificity of 93.33% using an SVM classifier with polynomial kernel order 2. Furthermore, we showed that the GRI (Table 2) is a highly effective and accurate tool to differentiate images taken from patients with glaucoma and normal participants. The index can also be employed to assess the efficacy of glaucoma medication.

## 8. Conclusion

In this work, we have presented a new automated glaucoma diagnosis system using a combination of HOS, TT, and DWT features extracted from digital fundus images. Our system, using an SVM classifier (with polynomial kernel order 2), was able to detect glaucoma and normal classes with an accuracy of 91.67%, sensitivity of 90%, and specificity of 93.33%. This classification efficiency may even be further improved

using images with a broader range of disease progression, better features, and robust data mining algorithms. In addition, we propose an integrated index, which is composed of HOS, TT, and DWT features. The GRI is a single feature which distinguishes normal and glaucoma fundus images, as shown in Table 2 and Fig. 7. Hence, it is a highly effective diagnostic tool which may help clinicians to make faster decisions during mass screening of retinal images.

The proposed system is cost-effective, because it integrates seamlessly with digital medical and administrative processes and incorporates inexpensive general processing components. Therefore, the glaucoma detection system can be used in mass screening where even a modest cost reduction, in the individual diagnosis, amounts to considerable cost savings. Such cost savings may help to eliminate suffering, because the money can be used to increase the pervasiveness of glaucoma screening or it can be used anywhere else in the health service, where it is even more effective.

## References

1. Bock R, Meier J, Nyúl LG, Hornegger J, Michelson G, Glaucoma risk index: Automated glaucoma detection from color fundus images, *Med Image Anal* **14**:471–481, 2010.
2. Glaucoma Research Foundation, Glaucoma facts and stats, Retrieved May 1, 2012, from [http://www.glaucoma.org/learn/glaucoma\\_facts.php](http://www.glaucoma.org/learn/glaucoma_facts.php).
3. Nyúl LG, Retinal image analysis for automated glaucoma risk evaluation, in Liu, J, Doi, K, Fenster, A, Chan, SC (eds.), *Medical Imaging, Parallel Processing of Images, and Optimization Techniques*, SPIE, pp. 1–9, 2009.
4. Acharya UR, Dua S, Du X, Vinitha Sree S, Chua CK, Automated diagnosis of glaucoma using texture and higher order spectra features, *IEEE Trans Inf Technol Biomed* **15**(3):449–455, 2011.
5. Mookiah MRK, Acharya UR, Lim CM, Petznick A, Suri JS, Data mining technique for automated diagnosis of glaucoma using higher order spectra and wavelet energy features, *Knowl-Based Syst* **33**(0):73–82, 2012.
6. Lin SC, Singh K, Jampel HD, Hodapp EA, Smith SD, Francis BA, Dueker DK, Fechtner RD, Samples JS, Schuman JS, Minckler DS, Optic nerve head and retinal nerve fiber layer analysis: A report by the american academy of ophthalmology, *Ophthalmology* **114**(10):1937–1949, 2007.
7. Staal J, Abramoff MD, Niemeijer M, Viergever MA, van Ginneken B, Ridge-based vessel segmentation in color images of the retina, *IEEE Trans Med Imaging* **23**(4):501–509, 2004.
8. Chrástek R, Wolf M, Donath K, Niemann H, Paulus D, Hothorn T, Lausen B, Lämmer R, Mardin CY, Michelson G, Automated segmentation of the optic nerve head for diagnosis of glaucoma, *Med Image Anal* **9**(4):297–314, 2005.
9. Hoover A, Goldbaum M, Locating the optic nerve in a retinal image using the fuzzy convergence of the blood vessels, *IEEE Trans Med Imaging* **22**(8):951–958, 2003.
10. Walter T, Klein J-C, Automatic detection of microaneurysms in color fundus images of the human retina by means of the bounding box closing, in *Proc of the 3rd Int Symp on Med Data Anal, ISMDA '02*, Springer-Verlag, London, UK, 2002, pp. 210–220.
11. Rapantzikos K, Zervakis ME, Balas K, Detection and segmentation of drusen deposits on human retina: Potential in the diagnosis of age-related macular degeneration, *Med Image Anal* **7**(1):95–108, 2003.

12. Yun WL, Acharya UR, Venkatesh YV, Chee C, Min LC, Ng EYK, Identification of different stages of diabetic retinopathy using retinal optical images, *Inf Sci* **178**(1):106–121, 2008.
13. Swindale NV, Stjepanovic G, Chin A, Mikelberg FS, Automated analysis of normal and glaucomatous optic nerve head topography images, *Invest Ophthalmol Vis Sci* **41**(7):1730–1742, 2000.
14. Abdel-Ghafar RA, Morris T, Ritchings T, Wood I, Detection and characterisation of the optic disk in glaucoma and diabetic retinopathy, *Proc MIUA 2004*, 2–5, 2004.
15. Uchida H, Brigatti L, Caprioli J, Detection of structural damage from glaucoma with confocal laser image analysis, *Invest Ophthalmol Vis Sci* **37**(12):2393–2401, 1996.
16. Iester M, Swindale NV, Mikelberg FS, Sector-based analysis of optic nerve head shape parameters and visual field indices in healthy and glaucomatous eyes, *J Glaucoma* **6**:371–376, 1997.
17. Zangwill LM, Chan K, Bowd C, Hao J, Lee T-W, Weinreb RN, Sejnowski TJ, Goldbaum MH, Heidelberg retina tomograph measurements of the optic disc and parapapillary retina for detecting glaucoma analyzed by machine learning classifiers, *Invest Ophthalmol Vis Sci* **45**(9):3144–3151, 2004.
18. Gonzalez RC, Woods RE, *Digital Image Processing*, Addison-Wesley Longman Publishing Co., Inc., Boston, MA, USA, 1992.
19. Kadyrov A, Petrou M, The trace transform and its applications, *IEEE Trans Pattern Anal Mach Intell* **23**(8):811–828, 2001.
20. Acharya UR, Chua CK, Ng EY, Yu W, Chee C, Application of higher order spectra for the identification of diabetes retinopathy stages, *J Med Syst* **32**(6):481–488, 2008.
21. Basile TMA, Caponetti L, Castellano G, Sforza G, A texture-based image processing approach for the description of human oocyte cytoplasm, *IEEE Trans Instrum Meas* **59**(10):2591–2601, 2010.
22. Szekely N, Toth N, Pataki B, A hybrid system for detecting masses in mammographic images, *IEEE Trans Instrum Meas* **55**(3):944–952, 2006.
23. Tan J-H, Ng EYK, Acharya UR, Chee C, Infrared thermography on ocular surface temperature: A review, *Infrared Phys Technol* **52**(4):97–108, 2009.
24. Acharya UR, Faust O, Sree VS, Molinari F, Garberoglio R, Suri JS, Cost-effective and non-invasive automated benign and malignant thyroid lesion classification in 3d contrast-enhanced ultrasound using combination of wavelets and textures: A class of thyroscan (tm) algorithms, *Technol Cancer Res Treat* **10**(4):371–80, 2011.
25. Stoitsis J, Golemati S, Nikita KS, Nicolaides AN, A modular software system to assist interpretation of medical images application to vascular ultrasound images, in: *Imaging Systems and Techniques, 2004 (IST), 2004 IEEE Int Workshop*, pp. 135–140, 2004.
26. Acharya UR, Chua EC, Chua KC, Min LC, Tamura T, Analysis and automatic identification of sleep stages using higher order spectra, *Int J Neural Syst* **20**(6):509–521, 2010.
27. Chua KC, Chandran V, Rajendra Acharya U, Lim CM, Analysis of epileptic eeg signals using higher order spectra, *J Med Eng Technol* **33**(1):42–50, 2009.
28. Chua KC, Chandran V, Acharya UR, Lim CM, Cardiac state diagnosis using higher order spectra of heart rate variability, *J Med Eng Technol* **32**(2):145–155, 2008.
29. Chandran V, Carswell B, Boashash B, Elgar S, Pattern recognition using invariants defined from higher order spectra: 2-d image inputs, *IEEE Trans Image Process* **6**(5):703–712, 1997.
30. Vetterli M, Herley C, Wavelets and filter banks: theory and design, *IEEE Trans Signal Process* **40**(9):2207–2232, 1992.
31. Ramesh R, Madheswaran M, Kannan K, Nanoscale finfet sensor for determining the breast cancer tissues using wavelet coefficients, *J Mech Med Biol* **11**:1295–1314, 2011.

32. Chourasia VS, Tiwari AK, Gangopadhyay R, Time-frequency characterization of fetal phonocardiographic signals using wavelet scalogram, *J Mech Med Biol* **11**:391–406, 2011.
33. Dua S, Acharya UR, Chowriappa P, Sree SV, Wavelet-based energy features for glaucomatous image classification, *IEEE Trans Inf Technol Biomed* **16**(1):80–87, 2012.
34. Yuan H, Gao J, Guo HZ, Lu C, An efficient method to process the quantized acousto-electric current: Wavelet transform, *IEEE Trans Instrum Meas* **60**(3):696–702, 2011.
35. Ren J, Ann vs. svm: Which one performs better in classification of mccs in mammogram imaging, *Know-Based Syst* **26**:144–153, 2012.
36. Vapnik VN, *The Nature of Statistical Learning Theory, Statistics for Engineering and Information Science*, Springer, 2000.
37. Martis RJ, Chakraborty C, Arrhythmia disease diagnosis using neural network, svm and genetic algorithm optimized k-means clustering, *J Mech Med Biol* **11**:897–915, 2011.
38. Nagarajan R, Balachandran C, Gunaratnam D, Klistorner A, Graham S, Neural network model for early detection of glaucoma using multi-focal visual evoked potential (m-vep), *Invest Ophthalmol Vis Sci* **43**(12):39–52, 2002.
39. Bizios D, Heijl A, Bengtsson B, Trained artificial neural network for glaucoma diagnosis using visual field data: A comparison with conventional algorithms, *J Glaucoma* **16**:20–28, 2007.
40. Nayak J, Acharya UR, Bhat PS, Shetty N, Lim T-C Automated diagnosis of glaucoma using digital fundus images, *J Med Syst* **33**(5):337–346, 2009.
41. Balasubramanian M, Žabic S, Bowd C, Thompson HW, Wolenski P, Iyengar SS, Karki BB, Zangwill LM, A framework for detecting glaucomatous progression in the optic nerve head of an eye using proper orthogonal decomposition, *Trans Inf Tech Biomed* **13**(5):781–793, 2009.
42. Huang M-L, Chen H-Y, Huang W-C, Tsai Y-Y, Linear discriminant analysis and artificial neural network for glaucoma diagnosis using scanning laser polarimetry variable cornea compensation measurements in taiwan chinese population, *Graefe's Arch Clin Exp Ophthalmol* **248**: 435–441, 2010.
43. Bock R, Meier J, Michelson G, Nyúl LG, Hornegger J, Classifying glaucoma with image-based features from fundus photographs, in *Proc of the 29th DAGM Conf on Pattern Recognition*, Springer-Verlag, Berlin, Heidelberg, 2007, pp. 355–364.
44. Muramatsu C, Hatanaka Y, Sawada A, Yamamoto T, Fujita H, Computerized detection of peripapillary chorioretinal atrophy by texture analysis, in *Engineering in Medicine and Biology Society, EMBC, 2011 Annu Int Conf of the IEEE*, pp. 5947–5950, 2011.
45. Kolar R, Jan J, Detection of glaucomatous eye via color fundus images using fractal dimensions, *Radio Eng* **17**: 109–114, 2008.